### APPLIED SCIENCES AND ENGINEERING

# Giant chiral amplification of chiral 2D perovskites via dynamic crystal reconstruction

Hongki Kim<sup>1,2</sup>†, Wonbin Choi<sup>1</sup>†, Yu Jin Kim<sup>3</sup>, Jihoon Kim<sup>4</sup>, Jaeyong Ahn<sup>1</sup>, Inho Song<sup>1,5</sup>, Minjoon Kwak<sup>1</sup>, Jongchan Kim<sup>1</sup>, Jonghyun Park<sup>1</sup>, Dongwon Yoo<sup>1,4</sup>, Jungwon Park<sup>1,4</sup>, Sang Kyu Kwak<sup>6</sup>\*, Joon Hak Oh<sup>1</sup>\*

Chiral hybrid perovskites show promise for advanced spin-resolved optoelectronics due to their excellent polarization-sensitive properties. However, chiral perovskites developed to date rely solely on the interaction between chiral organic ligand cations exhibiting point chirality and an inorganic framework, leading to a poorly ordered short-range chiral system. Here, we report a powerful method to overcome this limitation using dynamic long-range organization of chiral perovskites guided by the incorporation of chiral dopants, which induces strong interactions between chiral dopants and chiral cations. The additional interplay of chiral cations with chiral dopants reorganizes the morphological and crystallographic properties of chiral perovskites, notably enhancing the asymmetric behavior of chiral 2D perovskites by more than 10-fold, along with the highest dissymmetry factor of photocurrent ( $g_{Ph}$ ) of ~1.16 reported to date. Our findings present a pioneering approach to efficiently amplify the chiroptical response in chiral perovskites, opening avenues for exploring their potential in cutting-edge optoelectronic applications.



#### INTRODUCTION

Chiral materials interact strongly with the spin angular momentum (SAM) of photons when subjected to chiral electromagnetic fields, giving rise to circular dichroism (CD) or circularly polarized photoluminescence (CPPL). The former is the anisotropic absorption between right-handed circularly polarized light (RCPL) and left-handed circularly polarized light (LCPL), and the latter is due to anisotropic emission between RCPL and LCPL (1, 2). Integrating these functionalities into optoelectronic devices allows for various next-generation applications, ranging from chiral recognition and polarized imaging to optical quantum cryptography and optical communication (3–8). Therefore, there is a great deal of interest in constructing efficient SAM-active layers and leveraging them in cutting-edge applications.

Chiral two-dimensional (2D) organic-inorganic hybrid perovskites (OIHPs) are emerging as a promising class of SAM-active materials for chiral optoelectronics (e.g., CPL detectors or CPL emitters) due to their efficient spin-polarized charge transport, high absorption coefficient, and tunable bandgap (9, 10). Nevertheless, their weak optical activity and limited methodologies for boosting their chiroptical activity remain major obstacles that must be addressed to fully explore their potential applications. Chiroptical properties in existing chiral 2D OIHPs have primarily been driven by chiral transfer from chiral organic cations to inorganic sublattices (2). However, the coherent orientation of chiral organic cations is hindered by weak  $\pi$ - $\pi$  interactions

<sup>1</sup>School of Chemical and Biological Engineering, Institute of Chemical Processes, Seoul National University, Seoul 08826, Republic of Korea. <sup>2</sup>Department of Applied Physical Sciences, University of North Carolina at Chapel Hill, Chapel Hill, NC, USA. <sup>3</sup>School of Energy and Chemical Engineering, Ulsan National Institute of Science and Technology (UNIST), Ulsan 44919, Republic of Korea. <sup>4</sup>Center for Nanoparticle Research, Institute for Basic Science (IBS), Seoul National University, Seoul 08826, Republic of Korea. <sup>5</sup>Department of Chemistry, Purdue University, West Lafayette, IN, USA. <sup>6</sup>Department of Chemical and Biological Engineering, Korea University,

†These authors contributed equally to this work.

Seoul 02841, Republic of Korea.

in typical chiral 2D OIHPs, leading to inhomogeneous chirality transfer from chiral organic ligand cations to inorganic frameworks. Moreover, the lack of control over their ordering within inorganic frameworks during fast crystallization processes leads to the inevitable production of a poorly ordered chiral 2D OIHP system. This indicates an intrinsic limitation of conventional monolithic chiral organic cation–inorganic framework systems (MCIFs), driven solely by the monotonous interplay between chiral organic cations and inorganic frameworks

Several approaches to enhance and control the chiroptical properties of chiral 2D OIHPs have been developed: tailoring the molecular structure of chiral organic cations using a variety of chiral cations, such as R or S-methylbenzylammonium (R or S-MBA<sup>+</sup>) (11-16), R or S-methylphenethylammonium (R or S-MPA<sup>+</sup>) (17, 18), R or S-(naphthyl)ethylammonium (R or S-NEA<sup>+</sup>) (19, 20), and halide substituted R or S-X-MBA<sup>+</sup> (X = F, Cl, Br, I) (21–23); utilization of blends of chiral organic cation and achiral organic cations (24-26); introduction of subsidiary nanoporous templates or cavities (27–29); dimensionality engineering of perovskites (19, 30); introduction of additives (31); and controlling the compositional elements of perovskites (32, 33). However, these approaches have drawbacks, such as undesired inversion or peak shifts in the original CD spectra, challenges in device integration due to the introduction of extra structures (i.e., templates or cavities), and inefficient chiral amplification. Therefore, a powerful methodology is required to enhance the chirality of 2D perovskites in a more efficient and controllable manner while preserving the distinctive characteristics (such as sign and peak position) evident in the CD spectra.

Beyond the conventional MCIFs, we herein introduce additional chiral dopants [(2S,3S/2R,3R)-2,3-O-isopropylidene-1,1,4,4-tetraphenyl-1,2,3,4-butanetetrol, i.e., (+/-)-TADDOLs] into chiral 2D OIHPs with chiral organic ligand cations (R/S-MBA<sup>+</sup>). The additional interplay between chiral organic cations and chiral dopants leads to the dynamic crystal reconstruction in chiral 2D OIHPs, giving rise to intriguing phenomena. First, the appearance of unique spherulitic tornado-like morphologies with high homogeneity enables a long-range chiral activity.

<sup>\*</sup>Corresponding author. Email: joonhoh@snu.ac.kr (J.H.O.); skkwak@korea.ac.kr (S.K.K.)

Second, crystals in chiral 2D OIHPs undergo splintering into much smaller crystals under a compressive strain, promoting the lattice distortion in the inorganic frameworks. As a consequence of these advancements, the anisotropy factor of chiral 2D OIHP films with TADDOLs exhibits a remarkable chiral amplification effect without signal inversion or substantial shift on the CD spectra. Last, we have successfully implemented a self-powered CPL detector, achieving an outstanding  $g_{\rm Ph}$  surpassing 1. These results demonstrate a highly efficient and viable pathway to overcome the limitations of typical MCIFs by introducing a chiral dopant.

# **RESULTS**

# Long-range organization of chiral 2D OIHPs guided by chiral dopants

Unlike typical chiral cations (R/S-MBA<sup>+</sup>) with point chirality, a secondary chiral component (TADDOL) enables self-assembly to produce long-range chirality and distinctive morphologies due to the intermolecular interactions encompassing hydrogen bonding and  $\pi$ - $\pi$  stacking (figs. S1 and S2). Harnessing the unique properties of TADDOLs, we used a systematic design approach, hypothesizing that the morphological organization of chiral 2D OIHPs could potentially differ after introducing the TADDOLs compared to MCIFs. This divergence may occur given the potential additional interplay between TADDOLs and chiral organic cations (Fig. 1A).

To confirm this hypothesis, we investigated the morphologies of TADDOL-introduced (R/S-MBA)<sub>2</sub>PbI<sub>4</sub> films via scanning electron microscopy (SEM). After material verification on the single-crystal chiral 2D OIHP (fig. S3), we added TADDOLs into (R/S-MBA)<sub>2</sub>PbI<sub>4</sub> with controlled TADDOL-to-R/S-MBA<sup>+</sup> molar ratios. Upon adding (+)-TADDOL or (-)-TADDOL into (R-MBA)<sub>2</sub>PbI<sub>4</sub> or (S-MBA)<sub>2</sub>PbI<sub>4</sub>, spherulitic tornado-like morphologies appeared, in stark contrast to the pristine films (Fig. 1, B to D, and fig. S4). Without their introduction, (R/S-MBA)<sub>2</sub>PbI<sub>4</sub> thin films consisted of grains with discernible grain size and general shape. This morphology produced many pinholes in the film. On the other hand, chiral 2D OIHP films showed entirely reconstructed morphological properties after their introduction. Crystals were splintered into much smaller crystals with sizes that were difficult to discern, and a spherulitic tornado-like morphology extending from the central point was produced with much greater compactness and higher homogeneity compared to the pristine film. When adding (-)-TADDOL or (+)-TADDOL into (R-MBA)<sub>2</sub>PbI<sub>4</sub> or (S-MBA)<sub>2</sub>PbI<sub>4</sub>, respectively, similar morphologies were observed with splintered grains but with a slightly blurred spherulitic tornado-like morphology (fig. S5). The smaller crystal size with the addition of TADDOL was also confirmed via a transmission electron microscope (TEM) (fig. S6).

We attributed this to the effective suppression of macrocrystal formation through the interaction between TADDOLs and chiral amines, which facilitates the reconstruction of splintered crystals in a similar manner to the self-assembly of TADDOLs. Because of the presence of a halide helical screw parallel to the substrate in the symmetry-breaking distorted inorganic framework (fig. S7) (34), the introduction of TADDOLs and their homogeneous coassembly with chiral 2D OIHPs enables long-range chiral order with extended helical length of the halide screw. This eventually increases the local magnitude of magnetic fields (*B*), directly contributing to the anisotropy factor (35, 36). To scrutinize this phenomenon, we calculated the magnetic transition dipole moment

(|m|) and the rotational strength ( $R_{\rm eg}$ ) by obtaining the electric transition dipole moment ( $\mu$ ) and the asymmetry factor of CPPL ( $g_{\rm PL}$ ) (note S1, fig. S8, and table S1). Highly amplified |m| and  $R_{\rm eg}$  were obtained with the introduction of TADDOLs, intensifying |m| of (R-MBA)<sub>2</sub>PbI<sub>4</sub> [(S-MBA)<sub>2</sub>PbI<sub>4</sub>] from 0.0158  $\mu_{\rm B}$  (0.0131  $\mu_{\rm B}$ ) to 0.1388  $\mu_{\rm B}$  (0.1120  $\mu_{\rm B}$ ) and  $R_{\rm eg}$  of (R-MBA)<sub>2</sub>PbI<sub>4</sub> [(S-MBA)<sub>2</sub>PbI<sub>4</sub>] from 1.624 × 10<sup>-40</sup> erg esu cm G<sup>-1</sup> (1.333 × 10<sup>-40</sup> erg esu cm G<sup>-1</sup>) to 12.731 × 10<sup>-40</sup> erg esu cm G<sup>-1</sup> (12.311 × 10<sup>-40</sup> erg esu cm G<sup>-1</sup>) (Fig. 1, E to G).

# Chiroptical properties of chiral 2D OIHPs with chiral dopants

Next, we studied the chiroptical properties of TADDOL-introduced  $(R/S-MBA)_2PbI_4$  thin films. The features of the CD spectra of the reference (R/S-MBA)<sub>2</sub>PbI<sub>4</sub> were consistent with previous results (fig. S9) (21, 32), where the opposite signal values were obtained between (R-MBA)<sub>2</sub>PbI<sub>4</sub> and (S-MBA)<sub>2</sub>PbI<sub>4</sub>. The CD intensities of (R/S-MBA)<sub>2</sub>PbI<sub>4</sub> films were highly amplified after the introduction of TADDOLs (Fig. 2A). Specifically, the CD intensities of (-)-TADDOLintroduced (S-MBA)<sub>2</sub>PbI<sub>4</sub> film and (+)-TADDOL-introduced (R-MBA)<sub>2</sub>PbI<sub>4</sub> film were notably intensified from 15.576 mdeg at a wavelength of 495.5 nm to 219.117 mdeg at a wavelength of 486.0 nm and from −15.798 mdeg at a wavelength of 498 nm to −207.268 mdeg at a wavelength of 485.5 nm, respectively. The introduction of chiral molecules with the same structure as TADDOLs, except for the absence of benzene rings, did not amplify the chiral activity of chiral 2D OIHPs (fig. S10). These results suggest that chiral dopants with the  $\pi$ - $\pi$  stacking of the benzene rings play a crucial role in amplifying chiral activity. We also confirmed that the chiral amplification did not originate from the optical interference of thin film's linear birefringence (LB) and linear dichroism (LD) (i.e., LDLB effect), which can lead to the macroscopic anisotropic effect (27). To exclude LDLB effect, we observed the CD spectra of TADDOLintroduced chiral 2D OIHP films by flipping the sample by 180° with respect to the vertical axis. We confirmed that similar CD spectra were obtained when the sample was flipped (fig. S11), verifying the observed chiral amplification of TADDOL-introduced chiral 2D OIHP films originated from the intrinsic chiroptical property.

Chiroptical amplification was accompanied by several phenomena. First, weak hypsochromic shifts in absorbance were observed after introduction (fig. S12). This can be related to the induction of confinement in inorganic frameworks, which is discussed later. Second, exciton-coupled CD signals with bisignated Cotton effects strongly occurred. This was interpreted as a resonant coupling of excitons with the preferred magnitude and arrangement of the electric and magnetic transition dipole moments (37, 38). Along with strong Cotton effects, the amplification of all CD peaks assigned to each exciton transition demonstrated the effectiveness of TAD-DOLs as chiral amplifiers (fig. S13). Highly amplified  $|g_{CD}|$  of  $4.68 \times 10^{-3}$  [(R-MBA)<sub>2</sub>PbI<sub>4</sub> with (+)-TADDOL] and  $5.79 \times 10^{-3}$ [(S-MBA)<sub>2</sub>PbI<sub>4</sub> with (-)-TADDOL] were obtained compared to the  $|g_{CD}|$  for both reference  $(R\text{-MBA})_2\text{PbI}_4$  (3.70 × 10<sup>-4</sup>) and  $(S\text{-MBA})_2\text{PbI}_4$  $(3.30 \times 10^{-4})$  (Fig. 2B), which increased by more than 10-fold. This enhancement was among the highest chiral amplification effects reported for chiral 2D perovskite films without the use of additional templates or cavities, and it was achieved without inversion or substantial changes in the CD spectra (Fig. 2C and table S2). Highly amplified chiral anisotropic behavior was also confirmed by amplified CPPL intensities, with an improvement in the  $|g_{PL}|$ value from  $0.53 \times 10^{-3} (0.44 \times 10^{-3})$  for  $(R-MBA)_2PbI_4[(S-MBA)_2PbI_4]$ 

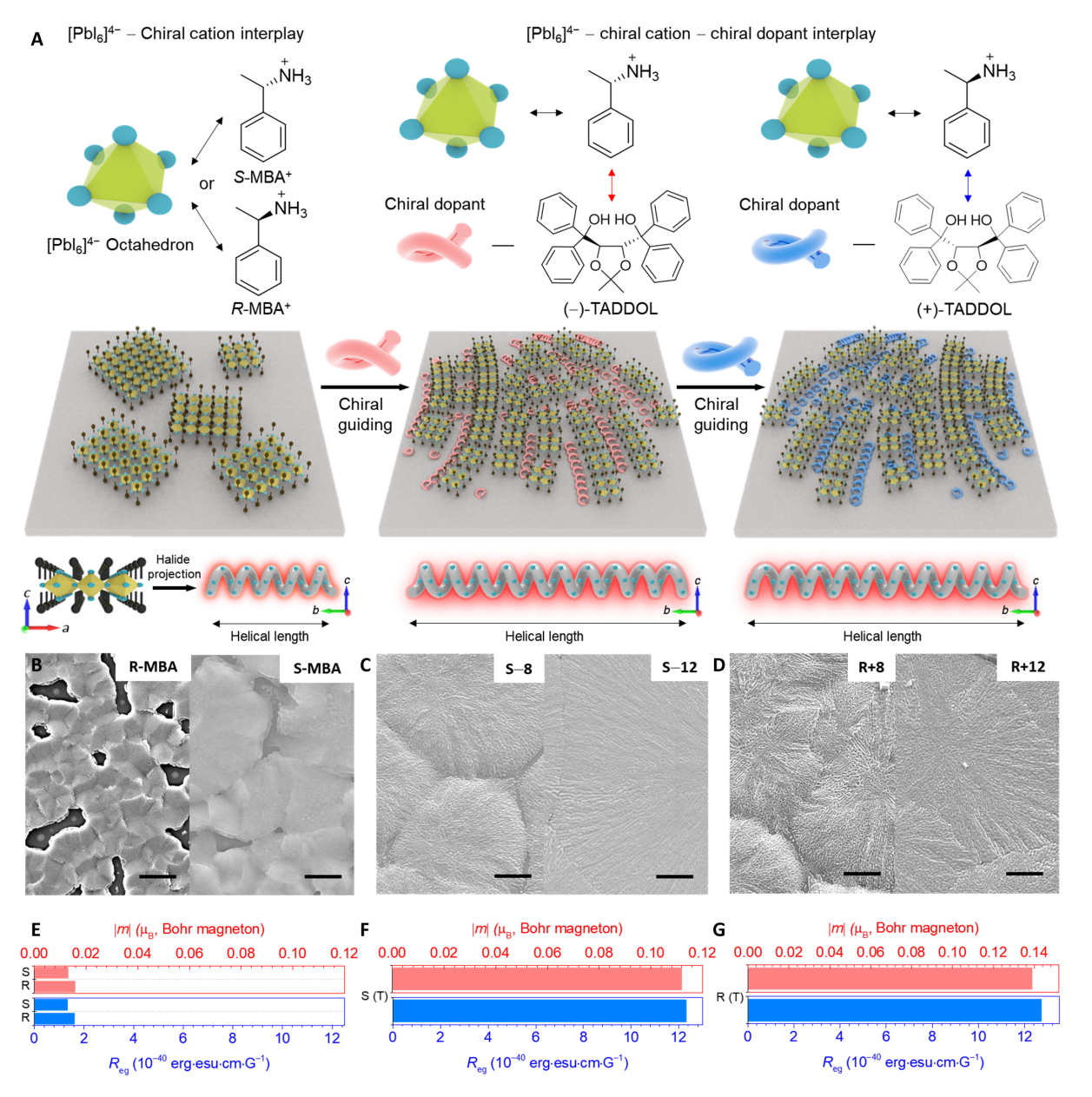


**Fig. 1. Long-range chiral model of chiral 2D OIHPs with TADDOLs. (A)** Schematic illustration of typical chiral 2D OIHPs driven by mono-interplay between chiral organic cations and inorganic frameworks and their evolution to long-range chiral assemblies driven by the additional interplay between chiral organic cations and TADDOLs. (**B** to **D**) SEM images of (B) pristine (S/R-MBA)<sub>2</sub>Pbl<sub>4</sub> films, (C) (–)-TADDOL (8 or 12%)–introduced (S-MBA)<sub>2</sub>Pbl<sub>4</sub> and (D) (+)-TADDOL (8 or 12%)–introduced (S-MBA)<sub>2</sub>Pbl<sub>4</sub> films. Inset scale bars in SEM images represent 2 μm. (**E** to **G**) Estimated |*m*| and  $R_{eg}$  of (E) pristine (S/R-MBA)<sub>2</sub>Pbl<sub>4</sub> films and (F) TADDOL-introduced (S-MBA)<sub>2</sub>Pbl<sub>4</sub> and (G) (S-MBA)<sub>2</sub>Pbl<sub>4</sub> films.

films to  $0.46 \times 10^{-2} (0.35 \times 10^{-2})$  for  $(R\text{-MBA})_2\text{PbI}_4$  with (+)-TADDOL [(S-MBA)<sub>2</sub>PbI<sub>4</sub> with (-)-TADDOL] films (fig. S14).

The *g*<sub>CD</sub> values and CD spectra with various doping concentrations of (+/-)-TADDOL and different combinations between (+/-)-TADDOLs and (*R*/*S*-MBA)<sub>2</sub>PbI<sub>4</sub> are summarized in Fig. 2D and fig. S15. A chirality amplification effect was clearly observed regardless of whether enantiomers of TADDOLs were used. (*R*-MBA)<sub>2</sub>PbI<sub>4</sub> films exhibited slightly higher *g*<sub>CD</sub> values when coupled with (+)-TADDOLs compared to (-)-TADDOLs. Conversely, (*S*-MBA)<sub>2</sub>PbI<sub>4</sub> films showed slightly higher

 $g_{\rm CD}$  values when coupled with (–)-TADDOLs compared to (+)-TADDOLs. It is also noteworthy that CD intensities of (R/S-MBA)<sub>2</sub>PbI<sub>4</sub> films were amplified after adding a racemic mixture of (+)-TADDOL and (–)-TADDOL (Fig. 2E), and the chiral activity of (rac-MBA)<sub>2</sub>PbI<sub>4</sub> films became active after the introduction of either one, showing CD spectra similar in magnitude and opposite in sign (Fig. 2F). This implies that equilibrating chiral conformer mixtures can be disturbed by the preferential interaction between (R/S-MBA)<sub>2</sub>PbI<sub>4</sub>and (+/–)-TADDOLs. Slightly different coupling strengths in enantiomeric pairs between R-MBA: (+)-TADDOL [S-MBA: (+)-TADDOL] and R-MBA:

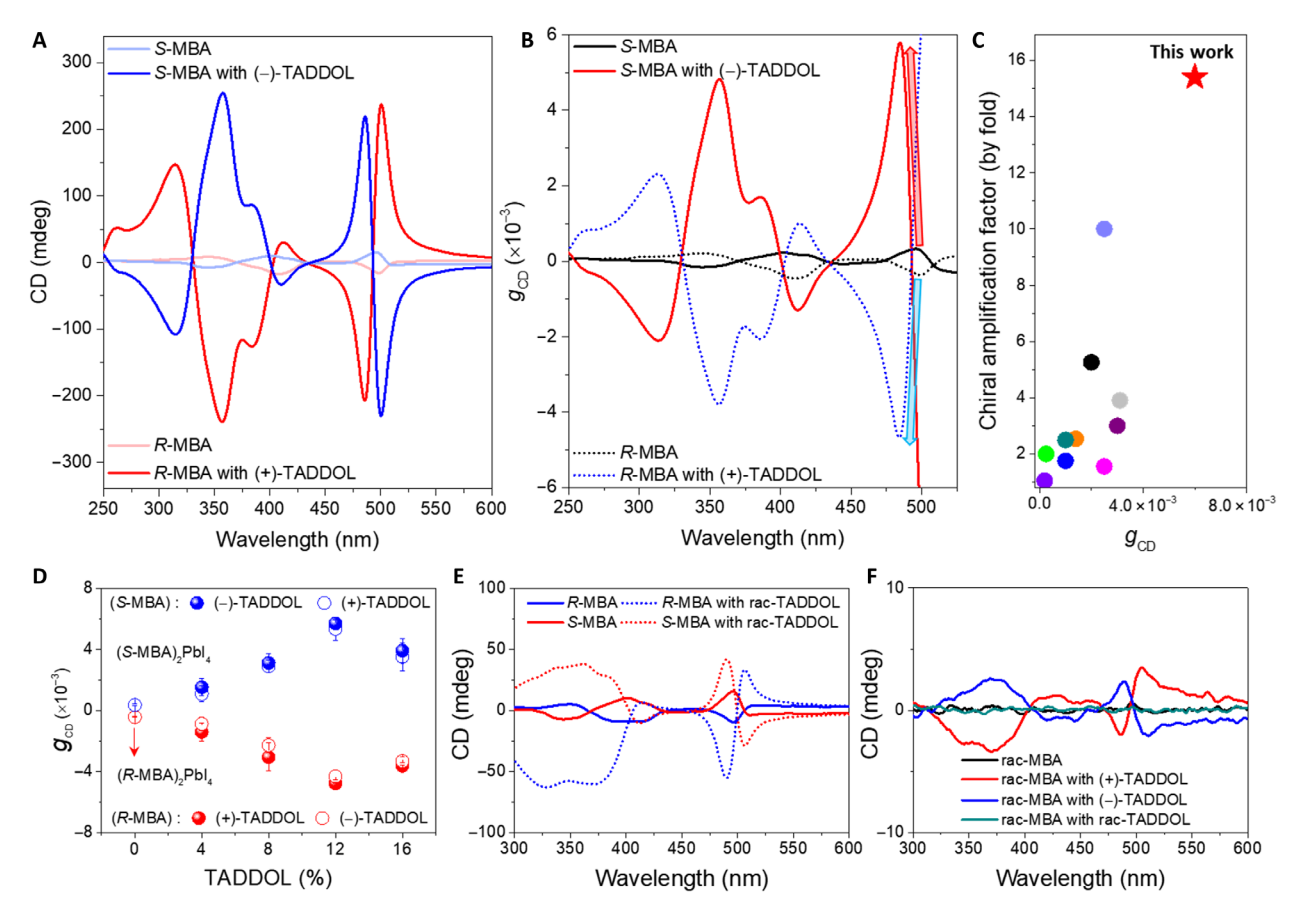


Fig. 2. Chiroptical properties of chiral 2D OIHPs with TADDOLs. (A and B) (A) CD spectra of  $(S-MBA)_2Pbl_4$  and  $(R-MBA)_2Pbl_4$  with or without the introduction of TADDOLs and (B) their corresponding  $g_{CD}$  spectra. (C) Correlation between chiral amplification factors with  $g_{CD}$  in reported studies for chiral 2D OIHPs (see table S2). (D) Statistical data of  $g_{CD}$  with different concentrations and combinations of (+/-)-TADDOLs. (E and F) CD spectra of (E) chiral 2D OIHP thin films with racemic TADDOL and (F) racemic 2D OIHP thin film with (+/-)-TADDOLs.

(-)-TADDOL [S-MBA: (-)-TADDOL)] may occur due to a small difference in the degree of steric interaction (39), but this requires further in-depth investigation.

# Crystallographic changes in chiral 2D OIHPs by chiral dopants

To examine the crystallographic properties of  $(R/S\text{-}MBA)_2\text{PbI}_4$  influenced by TADDOLs, x-ray diffraction (XRD) analysis was performed (fig. S16). The introduction of TADDOLs led to an increase in the full width at half maximum (FWHM) for the (002) plane peak in XRD, which in turn resulted in a decrease in crystallite size as calculated by the Scherrer equation (Fig. 3A). These crystallographic changes were consistent with the morphological results. The reduction in crystal sizes induced by TADDOLs was also evident in the sharper excitonic peaks observed in absorbance and slight increase in photoluminescence quantum yield, where smaller crystal sizes led to stronger exciton confinement (fig. S17). These results indicate that the crystal growth process of chiral 2D OIHPs was largely constrained by adding TADDOLs.

Next, we examined d-spacing and lattice microstrain variance with different concentrations of TADDOLs through Williamson-Hall analysis (Fig. 3B and figs. S18 and S19) (40). Notably, continuously increasing trends of d-spacing for the (002) plane of (R/S-MBA)<sub>2</sub>PbI<sub>4</sub>

were observed with TADDOLs. This may have been due to their interactions with chiral organic cations to affect the spatial distance of organic layers (i.e., interlayer distance between inorganic frameworks). This was supported by our x-ray photoelectron spectroscopy results, which showed no noticeable interaction between Pb and TADDOLs (fig. S20). The initial tensile strain of (*R*/S-MBA)<sub>2</sub>PbI<sub>4</sub> was progressively modulated toward compressive strain with the introduction of TADDOLs, which in turn induced octahedral tilting in the inorganic sublattices.

The structural changes in (MBA)<sub>2</sub>PbI<sub>4</sub> related to applied stress were traced by density functional theory (DFT) calculation (note S2 and figs. S21 and S22A). The biaxial compressive strain applied in the lateral direction (*a/b* lattice) induced a tensile strain in the *c* lattice, leading to an increase in *d*-spacing (fig. S22B). Consequently, the Pb-I-Pb angle decreased as the biaxial compressive strain was applied, indicating an increase in in-plane tilting of the inorganic octahedra (fig. S22C). Recent theoretical and experimental investigations have shown that imposing a higher degree of octahedral tilting in chiral 2D OIHPs (i.e., the distortion of Pb-I-Pb bonding angle) can promote chiral transfer by inducing stronger asymmetric hydrogen bonding between the chiral organic cation and inorganic framework (27, 34, 41, 42). This suggests that the introduction of TADDOLs not only promotes the long-range organization of chiral 2D OIHPs but

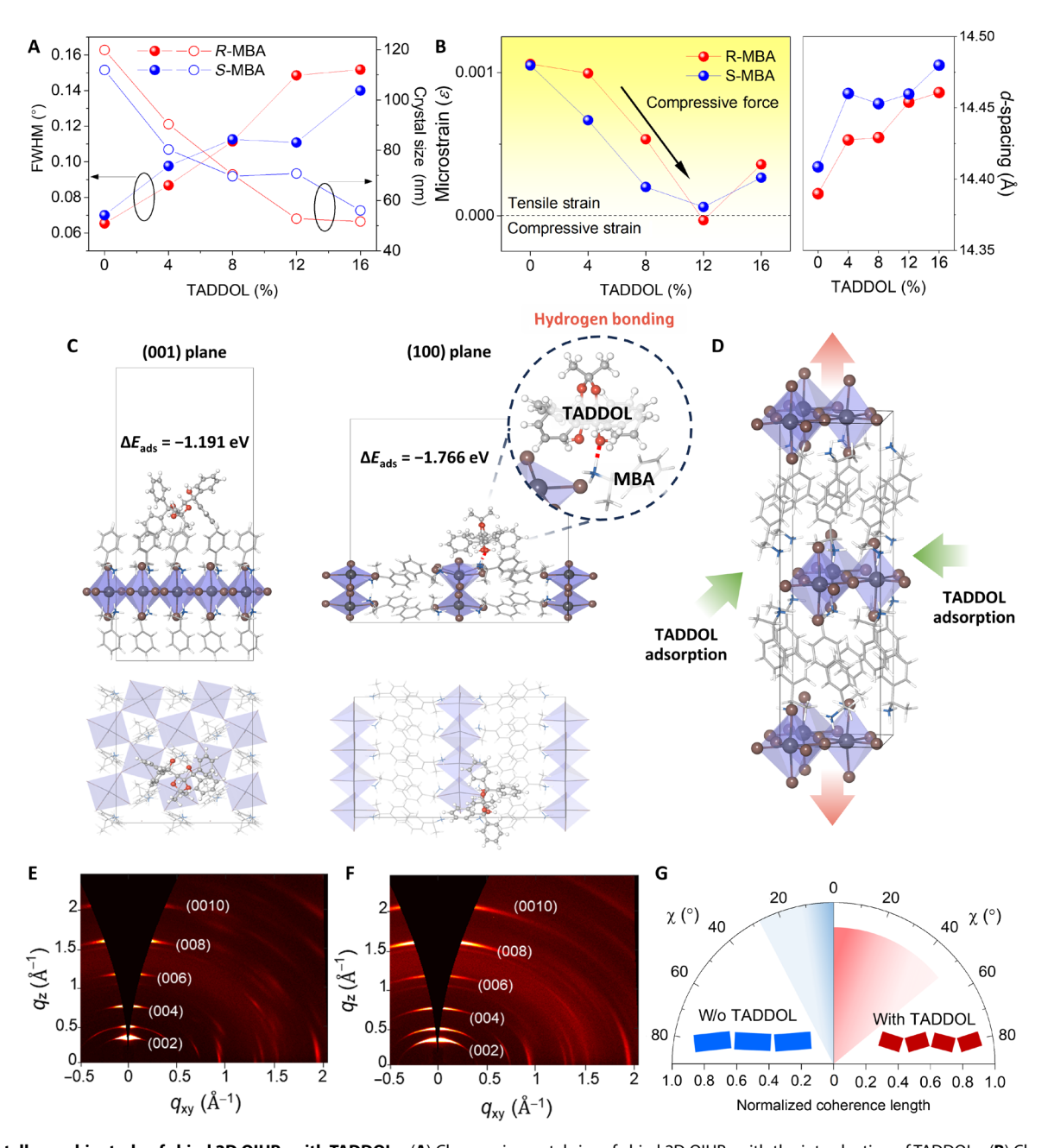


Fig. 3. Crystallographic study of chiral 2D OIHPs with TADDOLs. (A) Changes in crystal size of chiral 2D OIHPs with the introduction of TADDOLs. (B) Changes in microstrain (left) and d-spacing (right) of chiral 2D OIHPs with TADDOLs. (C) DFT calculations revealed adsorption directions and energies of TADDOLs on chiral 2D OIHPs. (D) Lattice expansion configuration in chiral 2D OIHPs induced by biaxial strain from TADDOL adsorption. (E and F) GWXS patterns and integrated azimuth angle plots of (002) diffraction of (E) the pristine (R-MBA)<sub>2</sub>Pbl<sub>4</sub> and (F) TADDOL-introduced (R-MBA)<sub>2</sub>Pbl<sub>4</sub> films. (G) Schematics displaying the crystal orientation based on integrated azimuth angle plots.

also induces octahedral tilting within these structures, both of which contribute to chiral amplification.

To probe the nature of interactions between chiral organic cations and TADDOLs, their adsorption configurations were investigated theoretically (note S2 and figs. S23 to S26). First, we investigated the interaction behavior between the MBA and TADDOL molecules. The amine group of the MBA molecule and the hydroxyl group of the TADDOL molecule demonstrated strong intermolecular hydrogen

bond formation, with a binding energy ( $\Delta E_{\text{bind}}$ ) of -2.260 eV (fig. S23A). This insight regarding hydrogen bonding may provide a basis for understanding the driving force behind the coassembly of TADDOLs and chiral 2D OIHPs.

Next, we investigated the surface of the (001) plane (in-plane direction) and the (100) plane (vertical direction) of pristine (MBA)<sub>2</sub>PbI<sub>4</sub> (fig. S25). Our calculations showed that the surface of the (001) plane was energetically more favorable with lower surface

energy of 0.00751 eV Å<sup>-2</sup> compared to the (100) plane surface  $(0.00909 \text{ eV Å}^{-2})$ , which aligns with the  $[PbI_6]^{4-}$  layer oriented parallel to the substrate (43). Then, we compared the adsorption energy of TADDOLs on these two planes (Fig. 3C). The (100) plane demonstrated a substantially stronger adsorption energy of -1.766 eV with the TADDOL, while the (001) plane showed an adsorption energy of -1.191 eV with the TADDOL. These observations suggest that TADDOLs find favorable adsorption sites on the (100) plane, as the exposed amine group of MBA facilitates hydrogen bonding with TADDOLs. On the other hand, the (001) plane revealed MBA to be oriented perpendicular to the surface, with the amine group buried and only the phenyl group exposed, thus hindering hydrogen bonding with TADDOLs. The results of DFT calculations corroborated these experimental findings, in which the lateral adsorption of TADDOLs to chiral 2D OIHPs, facilitated by hydrogen bonding between the exposed amine group of MBAs and TADDOLs, culminates in reduction of the crystal size under the influence of applied compressive strain (Fig. 3D).

Coassembly phenomena involving chiral 2D OIHPs and TAD-DOLs were also conjectured by the DFT calculations, which showed that the binding energy between the MBA and the TADDOL (i.e., -2.260 eV) was twice that between TADDOL molecules (i.e., -1.105 eV) (fig. S23). We further performed the grand canonical Monte Carlo simulations to confirm the feasibility of the prediction based on the molecular interaction strength. The additional TADDOL exhibited a tendency to preferentially adsorb to the amine group of MBA over the TADDOL in the cell (fig. S26). This provides theoretical evidence that the coassembly of TADDOL and

MBA molecules is more favorable than strong aggregation of TAD-DOL molecules among themselves.

To further investigate the impact of TADDOLs on crystallographic properties of chiral 2D OIHPs, grazing-incidence wideangle x-ray scattering (GIWAXS) patterns were obtained (Fig. 3, E and F, and fig. S27). The crystal orientation of chiral 2D OIHPs became more dynamically disordered after the introduction of TADDOLs, showing broadening of the integrated intensity plots azimuthally along the ring at  $q_r$  assigned to the (002) plane of corresponding films (fig. S28). The azimuth angle for the diffraction signal of the (002) plane was distributed from about  $-30^{\circ}$  to  $30^{\circ}$ , while it widened from to about -45° to 45° after adding TADDOLs with reduced coherence lengths (Fig. 3G and fig. S29). In contrast to horizontally oriented typical 2D OIHPs based on the continuous plate-like crystal structure in the lateral direction (44), the splintered crystals resulting from the penetration of TADDOLs restricted continuous crystal growth in the lateral direction. As a consequence, the splintered crystals exhibited a higher degree of freedom for tilting, contributing to their unique structural characteristics. This facilitated their coassembly with TADDOLs without inducing phase separation.

#### Chiral 2D OIHP-based CPL detectors

To demonstrate the effectiveness of chiral amplification in electronic devices, we fabricated a CPL detector with the device configuration: indium tin oxide (ITO)/chiral 2D OIHPs/MoO<sub>3</sub>/Au (Fig. 4A). The photocurrent characteristics under steady-state and real-time modes at zero bias demonstrated that polarization-dependent

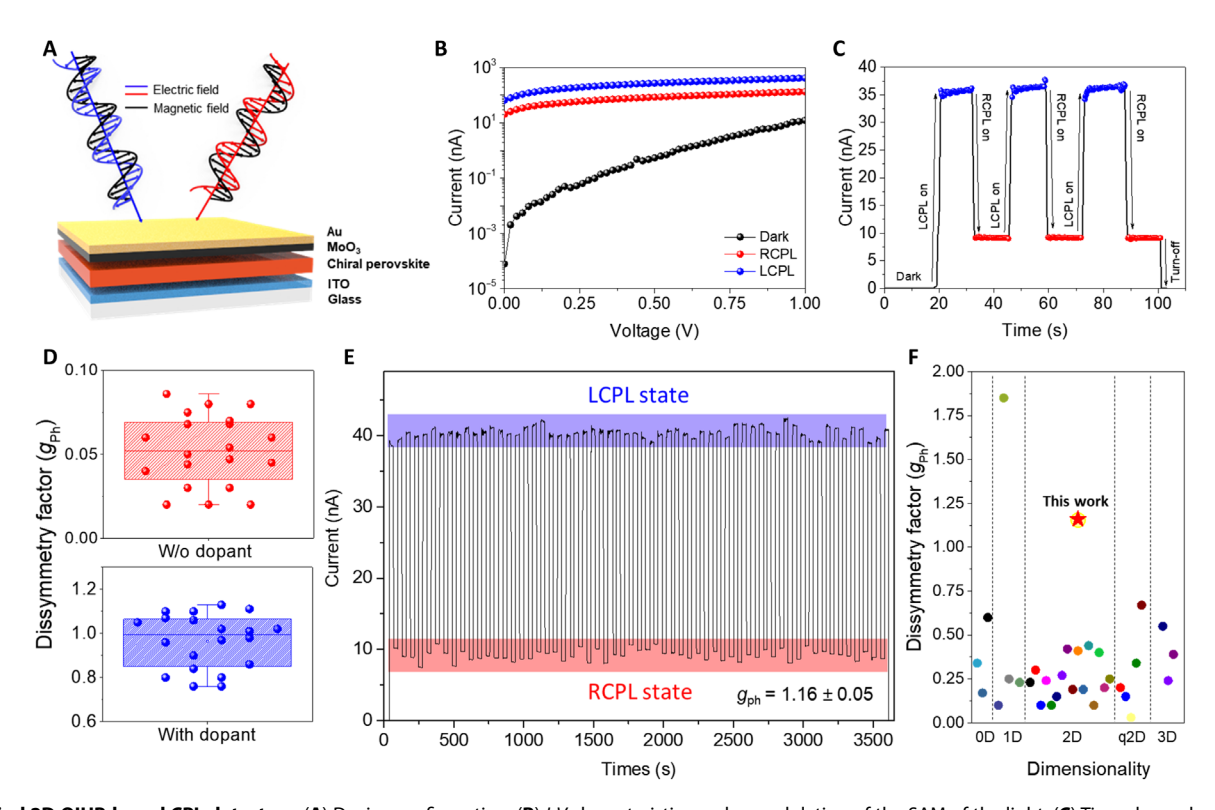


**Fig. 4. Chiral 2D OIHP-based CPL detectors.** (**A**) Device configuration. (**B**) *I-V* characteristics under modulation of the SAM of the light. (**C**) Time-dependent detection characteristics. (**D**) Statistics of  $g_{Ph}$  obtained from optimized 20 devices for each chiral 2D OIHP film. (**E**) Photocurrent monitoring during stepwise modulation of the SAM of the incident beam for 1 hour. (**F**) Comparison of this work with previous studies in terms of  $g_{Ph}$  and dimensionality (see table S3).

photon absorption resulted in notable differences in photocurrents depending on the SAM of the incident light at a wavelength of 491 nm (Fig. 4, B and C). The incorporation of chiral dopants endowed our system with a robust circular polarization detection ability at zero bias, yielding a remarkable  $g_{Ph}$  exceeding 1.1, which was also accompanied by notably enhanced specific detectivity  $(D^*)$ , photoresponsivity (R), and external quantum efficiency compared to the pristine device (figs. S30 and S31). TADDOL-introduced CPL detector also verified faster response time and higher linear dynamic range compared to the pristine device (figs. S32 and S33). Figure 4D reveals the higher and reproducible  $g_{Ph}$  afforded by the chiral dopant. The accuracy and reproducibility of SAM detection were further confirmed by monitoring photocurrent as a function of time during real-time stepwise modulation of the SAM of the incident beam for 1 hour, with an average  $g_{Ph}$  of 1.16 (Fig. 4E). The observed g<sub>Ph</sub> value far exceeded the state-of-the-art performance for chiral 2D OIHP-based CPL detectors (Fig. 4F and table S3), establishing an excellent correlation with the giant chiral amplification effect in absorbance.

#### **DISCUSSION**

We achieved highly amplified chiroptical activity in typical chiral 2D OIHPs through chiral dopant-assisted dynamic crystal reconstruction, which enabled strengthened lattice distortion and intriguing morphological evolution with a long-range chiral order. We found that the strong adsorption of chiral dopants to chiral organic cations plays a key role in inducing dynamic crystal reconstruction. Chiral 2D OIHP films with chiral dopants enabled highly sensitive discrimination of CPL with a greatly amplified  $g_{CD}$ , outperforming the limited chiroptical activity of typical MCIFs. The resulting CPL detectors exhibited remarkable sensitivity for SAM of incident photons in real time with  $g_{Ph}$  above 1.0 under zero bias, which is the highest value reported to date for chiral 2D OIHP-based CPL detectors. In contrast to existing MCIFs, our results provide a powerful tool for designing efficient chiral 2D OIHPs, thereby having a strong influence on the anisotropic behavior in chiral optoelectronics. Our findings will accelerate the development of advanced quantum cryptography and optical communication using the spin state control of light.

#### **MATERIALS AND METHODS**

#### Material

(R)-(+)-α-methylbenzylamine (R-MBA, 98%, optical purity > 97%), (S)-(-)-α-methylbenzylamine (S-MBA, 98%, optical purity > 97%), N,N-anhydrous dimethylformamide (DMF), anhydrous dimethyl sulfoxide (DMSO), lead oxide (PbO, 99.999%), and 57% aqueous hydriodic acid (HI) solution (99.95%, stabilized by H<sub>3</sub>PO<sub>2</sub>) were purchased from Sigma-Aldrich (St. Louis, MO, USA). Acetone (99.8%) and isopropanol (99.5%) were purchased from Daejung Chemical (Shiheung, Korea). (2S,3S/2R,3R)-2,3-O-isopropylidene-1,1,4,4-tetraphenyl-1,2,3,4-butanetetrol, (+/-)-TADDOLs were purchased from TCI Chemicals (Tokyo, Japan).

# Fabrication of chiral 2D OIHP films and CPL detectors

An amount of 0.5 g (2.2 mmol) PbO was fully dissolved in 3 ml of HI solution (57 wt %) and heated to 140°C with stirring at 1000 rpm. Then, 570  $\mu$ l of *R*- or *S*-MBA was reacted with 728  $\mu$ l of HI solution

in an ice bath for 20 min and added to this PbO/HI solution. The mixture was allowed to cool to room temperature under ambient conditions, resulting in the formation of orange crystals. The crystals were vacuum-filtrated, and the filtrate was rinsed with hexane several times. Last, the product was dried in a vacuum oven overnight. Then, the films were spin-coated on ITO glass substrates cleaned by sonication in deionized water/acetone/isopropanol for 10 min each and using an ultraviolet/ozone cleaner for 15 min. To prepare chiral 2D OIHP films, 60 µl of 0.3 M perovskite solution in DMF containing (+/-)-TADDOL at different molar ratios to chiral cations was spread on the ITO glass substrate, and spin coating was performed at 4000 rpm for 30 s. The spin-coated film was annealed at 100°C for 10 min on a hotplate. To fabricate vertically configured CPL detectors, chiral 2D OIHP polycrystalline film was fabricated by spin coating in the same way as described above on ITO glass. Then, a 4-nm-thick layer of MoO<sub>3</sub> and 20-nm-thick layer of Au were thermally evaporated under vacuum (<10<sup>-6</sup> mbar) in sequence to form an electrode (active area of 200 μm by 200 μm).

#### Film and device characterization

XRD analyses were conducted using an x-ray diffractometer (Smart Lab, Rigaku, Tokyo, Japan) with Cu K $\alpha$  radiation ( $\lambda = 1.5406 \text{ Å}$ ) at 40 kV/40 mA. SEM was performed using a field emission SEM (JSM-7800F Prime; JEOL, Tokyo, Japan). TEM images were acquired using a JEM-ARM200F (JEOL) electron microscope installed at the National Center for Inter-university Research Facility at Seoul National University. The microscope was equipped with a cold emission gun, a spherical aberration corrector at image-forming lens, and a direct electron detector (K3-IS; Gatan, Pleasanton, CA, USA). TEM imaging was performed with an electron dose rate of 10 to 20 e<sup>-</sup> Å<sup>-2</sup> s<sup>-1</sup> to alleviate structural degradation of the sample. GIWAXS measurements were conducted on the PLS-II 9A U-SAXS beamline at the Pohang Accelerator Laboratory in Korea. X-rays emitted from the in-vacuum undulator were monochromated at 11.025 keV  $(\lambda = 1.12454 \text{ Å})$  using a double-crystal monochromator and then focused both horizontally and vertically [450 μm (H) by 60 μm (V) in the FWHM sample position] using K-B-type mirrors. The sample stage was equipped with a seven-axis motorized stage for fine alignment of the sample, and the incidence angle of the x-ray beam was set to a range of 0.12° for structural analysis, which was close to the critical angle of the samples. The patterns were recorded with a 2D chargecoupled device detector (SX165; Rayonix, Evanston, IL, USA); the x-ray irradiation time ranged from 30 to 60 s according to the saturation level of the detector. Diffraction angles were calibrated using precalibrated sucrose (monoclinic,  $P2_1$ , a = 10.8631 Å, b = 8.7044 Å,  $c = 7.7624 \text{ Å}, \beta = 102.938^{\circ}$ ), and the sample-to-detector distance was ~220.8 mm. Absorption spectra were measured using an ultraviolet/ visible light spectrophotometer (V-770; Jasco, Tokyo, Japan). *I–V* and *I–t* curves were measured under vacuum using a parametric analyzer (4200-SCS; Keithley, Solon, OH, USA). CPL illumination was generated using a linear polarizer and a quarter-wave plate (Thorlabs, Newton, NJ, USA) installed between the light source and sample. The CPL direction of the laser light was controlled by wave plate rotation. CD spectroscopy was performed using a CD spectropolarimeter (J-815; Jasco). The  $g_{CD}$ , indicating the ratio of CD to conventional absorption, was calculated using the following equation

$$g_{\rm CD} = 2 \frac{A_{\rm L} - A_{\rm R}}{A_{\rm L} + A_{\rm R}} = \frac{\rm CD}{32980 \times A}$$

where  $A_L$  is the absorption for LCPL,  $A_R$  is the absorption for RCPL, CD is the value extracted from CD spectroscopy, and A is the absorbance of the sample. The  $g_{PL}$  was defined as

$$g_{\rm PL} = 2 \frac{I_{\rm PL,L} - I_{\rm PL,R}}{I_{\rm PL,L} + I_{\rm PL,R}}$$

where  $I_{\rm PL,L}$  and  $I_{\rm PL,R}$  indicate the photoluminescence emission intensity of LCPL and RCPL, respectively. The discrimination ability for CPL light of CPL detectors was characterized by  $g_{\rm Ph}$  in analogy to  $g_{\rm CD}$  as follows

$$g_{\text{Ph}} = \frac{2(I_{\text{Ph,L}} - I_{\text{Ph,R}})}{(I_{\text{Ph,L}} + I_{\text{Ph,R}})}$$

where  $I_{Ph,L}$  and  $I_{Ph,R}$  are the photocurrents under LCPL and RCPL illumination, respectively.

### **Supplementary Materials**

#### This PDF file includes:

Supplementary Notes S1 and S2 Figs. S1 to S33 Tables S1 to S3 References

#### **REFERENCES AND NOTES**

- J. Crassous, M. J. Fuchter, D. E. Freedman, N. A. Kotov, J. Moon, M. C. Beard, S. Feldmann, Materials for chiral light control. Nat. Rev. Mater. 8, 365–371 (2023).
- G. Long, R. Sabatini, M. I. Saidaminov, G. Lakhwani, A. Rasmita, X. Liu, E. H. Sargent, W. Gao. Chiral-perovskite optoelectronics. *Nat. Rev. Mater.* 5, 423–439 (2020).
- M. Hu, Y.-X. Yuan, W. Wang, D.-M. Li, H.-C. Zhang, B.-X. Wu, M. Liu, Y.-S. Zheng, Chiral recognition and enantiomer excess determination based on emission wavelength change of AlEgen rotor. *Nat. Commun.* 11, 161 (2020).
- L. Pu, Fluorescence of organic molecules in chiral recognition. Chem. Rev. 104, 1687–1716 (2004).
- I. Song, J. Ahn, H. Ahn, S. H. Lee, J. Mei, N. A. Kotov, J. H. Oh, Helical polymers for dissymmetric circularly polarized light imaging. *Nature* 617, 92–99 (2023).
- P. Stachelek, L. MacKenzie, D. Parker, R. Pal, Circularly polarised luminescence laser scanning confocal microscopy to study live cell chiral molecular interactions. *Nat. Commun.* 13, 553 (2022).
- D. de Bernardis, F. Piccioli, P. Rabl, I. Carusotto, Chiral quantum optics in the bulk of photonic quantum hall systems. PRX Quantum 4, 030306 (2023).
- X. Ma, M. Pu, X. Li, C. Huang, Y. Wang, W. Pan, B. Zhao, J. Cui, C. Wang, Z. Zhao, X. Luo, A planar chiral meta-surface for optical vortex generation and focusing. Sci. Rep. 5, 10365 (2015).
- J. Ma, H. Wang, D. Li, Recent progress of chiral perovskites: Materials, synthesis, and properties. Adv. Mater. 33, e2008785 (2021).
- A. Pietropaolo, A. Mattoni, G. Pica, M. Fortino, G. Schifino, G. Grancini, Rationalizing the design and implementation of chiral hybrid perovskites. Chem 8, 1231–1253 (2022).
- J. Ma, C. Fang, C. Chen, L. Jin, J. Wang, S. Wang, J. Tang, D. Li, Chiral 2D perovskites with a high degree of circularly polarized photoluminescence. ACS Nano 13, 3659–3665 (2019).
- H. Lu, J. Wang, C. Xiao, X. Pan, X. Chen, R. Brunecky, J. J. Berry, K. Zhu, M. C. Beard, Z. V. Vardeny, Spin-dependent charge transport through 2D chiral hybrid lead-iodide perovskites. Sci. Adv. 5, eaay0571 (2019).
- G. Long, C. Jiang, R. Sabatini, Z. Yang, M. Wei, L. N. Quan, Q. Liang, A. Rasmita, M. Askerka, G. Walters, X. Gong, J. Xing, X. Wen, R. Quintero-Bermudez, H. Yuan, G. Xing, X. R. Wang, D. Song, O. Voznyy, M. Zhang, S. Hoogland, W. Gao, Q. Xiong, E. H. Sargent, Spin control in reduced-dimensional chiral perovskites. *Nat. Photonics* 12, 528–533 (2018).
- J. Ahn, E. Lee, J. Tan, W. Yang, B. Kim, J. Moon, A new class of chiral semiconductors: Chiralorganic-molecule-incorporating organic-inorganic hybrid perovskites. *Mater. Horiz.* 4, 851–856 (2017).
- Y. Zhao, Y. Qiu, J. Feng, J. Zhao, G. Chen, H. Gao, Y. Zhao, L. Jiang, Y. Wu, Chiral 2D-perovskite nanowires for stokes photodetectors. J. Am. Chem. Soc. 143, 8437–8445 (2021).
- C. Chen, L. Gao, W. Gao, C. Ge, X. Du, Z. Li, Y. Yang, G. Niu, J. Tang, Circularly polarized light detection using chiral hybrid perovskite. *Nat. Commun.* 10, 1927 (2019).

- D. Li, X. Liu, W. Wu, Y. Peng, S. Zhao, L. Li, M. Hong, J. Luo, Chiral lead-free hybrid perovskites for self-powered circularly polarized light detection. *Angew. Chem. Int. Ed.* 60, 8415–8418 (2021).
- L. Wang, Y. Xue, M. Cui, Y. Huang, H. Xu, C. Qin, J. Yang, H. Dai, M. Yuan, A chiral reduced-dimension perovskite for an efficient flexible circularly polarized light photodetector. *Angew. Chem. Int. Ed.* 132, 6504–6512 (2020).
- A. Ishii, T. Miyasaka, Direct detection of circular polarized light in helical 1D perovskitebased photodiode. Sci. Adv. 6, eabd3274 (2020).
- J. Son, S. Ma, Y.-K. Jung, J. Tan, G. Jang, H. Lee, C. U. Lee, J. Lee, S. Moon, W. Jeong, A. Walsh, J. Moon, Unraveling chirality transfer mechanism by structural isomer-derived hydrogen bonding interaction in 2D chiral perovskite. *Nat. Commun.* 14, 3124 (2023).
- J.-T. Lin, D.-G. Chen, L.-S. Yang, T.-C. Lin, Y.-H. Liu, Y.-C. Chao, P.-T. Chou, C.-W. Chiu, Tuning the circular dichroism and circular polarized luminescence intensities of chiral 2D hybrid organic–inorganic perovskites through halogenation of the organic ions. *Angew. Chem. Int. Ed.* 60, 21434–21440 (2021).
- Y. Peng, X. Liu, L. Li, Y. Yao, H. Ye, X. Shang, X. Chen, J. Luo, Realization of vis–NIR dual-modal circularly polarized light detection in chiral perovskite bulk crystals. *J. Am. Chem. Soc.* 143, 14077–14082 (2021).
- J. Zhao, H. Huo, Y. Zhao, Y. Guo, M. Dong, Y. Fu, J. Zhang, Z. Gao, L. Kang, Chiral hybrid perovskites (R-/S-CLPEA)<sub>4</sub>Bi<sub>2</sub>I<sub>10</sub> with enhanced chirality and spin-orbit coupling splitting for strong nonlinear optical circular dichroism and spin selectivity effects. Chem. Mater. 35, 4347–4354 (2023).
- S. You, P. Yu, T. Zhu, Q. Guan, J. Wu, H. Dai, H. Zhong, Z.-K. Zhu, J. Luo, Alternating chiral and achiral spacers for constructing two-dimensional chiral hybrid perovskites toward circular-polarization-sensitive photodetection. *Mater. Horiz.* 10, 5307–5312 (2023).
- L. Yan, M. K. Jana, P. C. Sercel, D. B. Mitzi, W. You, Alkyl-aryl cation mixing in chiral 2D perovskites. J. Am. Chem. Soc. 143, 18114–18120 (2021).
- R. Lu, Z. Wen, M. Zhao, J. Li, L. Zhang, Y. Yang, H. Jin, Y. Chen, S. Wang, S. Pan, Spacer cation alloying enables markedly improved chiroptical properties of two-dimensional chiral hybrid perovskite nanosheets. *Adv. Opt. Mater.* 11, 2202290 (2023).
- S. Ma, Y.-K. Jung, J. Ahn, J. Kyhm, J. Tan, H. Lee, G. Jang, C. U. Lee, A. Walsh, J. Moon, Elucidating the origin of chiroptical activity in chiral 2D perovskites through nanoconfined growth. *Nat. Commun.* 13, 3259 (2022).
- S. Kim, S.-C. An, Y. Kim, Y. S. Shin, A. A. Antonov, I. C. Seo, B. H. Woo, Y. Lim, M. V. Gorkunov, Y. S. Kivshar, J. Y. Kim, Y. C. Jun, Chiral electroluminescence from thin-film perovskite metacavities. *Sci. Adv.* 9, eadh0414 (2023).
- Z. Wang, C.-C. Lin, K. Murata, A. S. A. Kamal, B.-W. Lin, M.-H. Chen, S. Tang, Y.-L. Ho, C.-C. Chen, C.-W. Chen, H. Daiguji, K. Ishii, J.-J. Delaunay, Chiroptical response inversion and enhancement of room-temperature exciton-polaritons using 2D chirality in perovskites. *Adv. Mater.* 35, e2303203 (2023).
- T. Zhu, W. Weng, C. Ji, X. Zhang, H. Ye, Y. Yao, X. Li, J. Li, W. Lin, J. Luo, Chain-to-layer dimensionality engineering of chiral hybrid perovskites to realize passive highly circular-polarization-sensitive photodetection. J. Am. Chem. Soc. 144, 18062–18068 (2022).
- C. U. Lee, S. Ma, J. Ahn, J. Kyhm, J. Tan, H. Lee, G. Jang, Y. S. Park, J. Yun, J. Lee, J. Son, J.-S. Park, J. Moon, Tailoring the time-averaged structure for polarization-sensitive chiral perovskites. *J. Am. Chem. Soc.* 144, 16020–16033 (2022).
- J. Ahn, S. Ma, J.-Y. Kim, J. Kyhm, W. Yang, J. A. Lim, N. A. Kotov, J. Moon, Chiral 2D organic inorganic hybrid perovskite with circular dichroism tunable over wide wavelength range. J. Am. Chem. Soc. 142, 4206–4212 (2020).
- B. Yao, Q. Wei, Y. Yang, W. Zhou, X. Jiang, H. Wang, M. Ma, D. Yu, Y. Yang, Z. Ning, Symmetry-broken 2D lead–tin mixed chiral perovskite for high asymmetry factor circularly polarized light detection. *Nano Lett.* 23, 1938–1945 (2023).
- M. K. Jana, R. Song, H. Liu, D. R. Khanal, S. M. Janke, R. Zhao, C. Liu, Z. Valy Vardeny,
  V. Blum, D. B. Mitzi, Organic-to-inorganic structural chirality transfer in a 2D hybrid perovskite and impact on Rashba-Dresselhaus spin-orbit coupling. *Nat. Commun.* 11, 4699 (2020).
- J. Lu, Y. Xue, K. Bernardino, N.-N. Zhang, W. R. Gomes, N. S. Ramesar, S. Liu, Z. Hu, T. Sun, A. F. de Moura, N. A. Kotov, K. Liu, Enhanced optical asymmetry in supramolecular chiroplasmonic assemblies with long-range order. *Science* 371, 1368–1374 (2021).
- C.-S. Ho, A. Garcia-Etxarri, Y. Zhao, J. Dionne, Enhancing enantioselective absorption using dielectric nanospheres. ACS Photonics 4, 197–203 (2017).
- G. Bhat, A. Roth, R. Day, Extrinsic cotton effect and helix-coil transition in a DNApolycation complex. *Biomolecules* 16, 1713–1724 (1977).
- N. Holmgaard List, J. Knoops, J. Rubio-Magnieto, J. Idé, D. Beljonne, P. Norman, M. Surin, M. Linares, Origin of DNA-induced circular dichroism in a minor-groove binder. J. Am. Chem. Soc. 139, 14947–14953 (2017).
- M. Anyika, H. Gholami, K. D. Ashtekar, R. Acho, B. Borhan, Point-to-axial chirality transfer—A new probe for "sensing" the absolute configurations of monoamines. J. Am. Chem. Soc. 136, 550–553 (2014).
- G. Williamson, W. Hall, X-ray line broadening from filed aluminium and wolfram. Acta Metall. 1, 22–31 (1953).

# SCIENCE ADVANCES | RESEARCH ARTICLE

- H. Lu, C. Xiao, R. Song, T. Li, A. E. Maughan, A. Levin, R. Brunecky, J. J. Berry, D. B. Mitzi, V. Blum, M. C. Beard, Highly distorted chiral two-dimensional tin iodide perovskites for spin polarized charge transport. *J. Am. Chem. Soc.* 142, 13030–13040 (2020).
- Y.-H. Kim, R. Song, J. Hao, Y. Zhai, L. Yan, T. Moot, A. F. Palmstrom, R. Brunecky, W. You, J. J. Berry, J. L. Blackburn, M. C. Beard, V. Blum, J. M. Luther, The structural origin of chiroptical properties in perovskite nanocrystals with chiral organic ligands. *Adv. Funct. Mater.* 32, 2200454 (2022).
- S. Najman, H.-A. Chen, H.-Y. T. Chen, C.-W. Pao, Surface structures and equilibrium shapes of layered 2D Ruddlesden-Popper perovskite crystals from density functional theory calculations. *Mater. Today Commun.* 26, 101745 (2021).
- P. Kovaricek, P. Nadazdy, E. Pluharova, A. Brunova, R. Subair, K. Vegso, V. L. P. Guerra,
  O. Volochanskyi, M. Kalbac, A. Krasnansky, P. Pandit, S. V. Roth, A. Hinderhofer, E. Majkova,
  M. Jergel, J. Tian, F. Schreiber, P. Siffalovic, Crystallization of 2D hybrid organic-inorganic perovskites templated by conductive substrates. Adv. Funct. Mater. 31, 2009007 (2021).
- N. S. S. Nizar, M. Sujith, K. Swathi, C. Sissa, A. Painelli, K. G. Thomas, Emergent chiroptical properties in supramolecular and plasmonic assemblies. *Chem. Soc. Rev.* 50, 11208– 11226 (2021)
- D. di Nuzzo, L. Cui, J. L. Greenfield, B. Zhao, R. H. Friend, S. C. J. Meskers, Circularly polarized photoluminescence from chiral perovskite thin films at room temperature. ACS Nano 14, 7610–7616 (2020).
- M. S. Alias, I. Dursun, M. I. Saidaminov, E. M. Diallo, P. Mishra, T. K. Ng, O. M. Bakr, B. S. Ooi, Optical constants of CH<sub>3</sub>NH<sub>3</sub>PbBr<sub>3</sub> perovskite thin films measured by spectroscopic ellipsometry. Opt. Express 24, 16586–16594 (2016).
- G. Kresse, J. Furthmüller, Efficiency of ab-initio total energy calculations for metals and semiconductors using a plane-wave basis set. Comput. Mater. Sci. 6, 15–50 (1996).
- G. Kresse, J. Furthmüller, Efficient iterative schemes for ab initio total-energy calculations using a plane-wave basis set. *Phys. Rev. B* 54, 11169–11186 (1996).
- J. P. Perdew, K. Burke, M. Ernzerhof, Generalized gradient approximation made simple. Phys. Rev. Lett. 77, 3865–3868 (1996).
- G. Kresse, D. Joubert, From ultrasoft pseudopotentials to the projector augmented-wave method. *Phys. Rev. B* 59, 1758–1775 (1999).
- S. Grimme, J. Antony, S. Ehrlich, H. Krieg, A consistent and accurate ab initio parametrization of density functional dispersion correction (DFT-D) for the 94 elements H-Pu. J. Chem. Phys. 132, 154104 (2010).
- H. J. Monkhorst, J. D. Pack, Special points for Brillouin-zone integrations. Phys. Rev. B 13, 5188–5192 (1976)
- D. G. Billing, A. Lemmerer, Synthesis and crystal structures of inorganic-organic hybrids incorporating an aromatic amine with a chiral functional group. CrstEngComm 8, 686–695 (2006).
- 55. D. Systèmes, Biovia materials studio. (Dassault Systèmes, 2019).
- H. Sun, Z. Jin, C. Yang, R. L. C. Akkermans, S. H. Robertson, N. A. Spenley, S. Miller, S. M. Todd, COMPASS II: Extended coverage for polymer and drug-like molecule databases. J. Mol. Model. 22, 47 (2016).
- B. Delley, An all-electron numerical method for solving the local density functional for polyatomic molecules. J. Chem. Phys. 92, 508–517 (1990).
- S. Grimme, Semiempirical GGA-type density functional constructed with a long-range dispersion correction. J. Comput. Chem. 27, 1787–1799 (2006).
- A. K. Rappe, C. J. Casewit, K. Colwell, W. A. Goddard III, W. M. Skiff, UFF, a full periodic table force field for molecular mechanics and molecular dynamics simulations. *J. Am. Chem.* Soc. 114, 10024–10035 (1992).
- R. S. Mulliken, Electronic population analysis on LCAO–MO molecular wave functions. I. J. Chem. Phys. 23, 1833–1840 (1955).
- Y. H. Lee, I. Song, S. H. Kim, J. H. Park, S. O. Park, J. H. Lee, Y. Won, K. Cho, S. K. Kwak, J. H. Oh, Perovskite granular wire photodetectors with ultrahigh photodetectivity. *Adv. Mater.* 32, 202002357 (2020).
- Y. Xie, J. Morgenstein, B. G. Bobay, R. Song, N. A. M. S. Caturello, P. C. Sercel, V. Blum,
  D. B. Mitzi, Chiral cation doping for modulating structural symmetry of 2D perovskites.
  J. Am. Chem. Soc. 145, 17831–17844 (2023).
- H. Zhu, Q. Wang, K. Sun, W. Chen, J. Tang, J. Hao, Z. Wang, J. Sun, W. C. H. Choy,
  P. Müller-Buschbaum, X. W. Sun, D. Wu, K. Wang, Solvent modulation of chiral perovskite films enables high circularly polarized luminescence performance from chiral perovskite/quantum dot composites. ACS Appl. Mater. Interfaces 15, 9978–9986 (2023).
- L. Scalon, J. Brunner, M. G. D. Guaita, R. Szostak, M. Albaladejo-Siguan, T. Kodalle,
  L. A. Guerrero-León, C. M. Sutter-Fella, C. C. Oliveira, Y. Vaynzof, A. F. Nogueira, Tuning phase purity in chiral 2D perovskites. *Adv. Opt. Mater.* 12, 2300776 (2023).
- H. Kim, R. M. Kim, S. D. Namgung, N. H. Cho, J. B. Son, K. Bang, M. Choi, S. K. Kim, K. T. Nam, J. W. Lee, J. H. Oh, Ultrasensitive near-infrared circularly polarized light detection using 3D perovskite embedded with chiral plasmonic nanoparticles. *Adv. Sci.* 9, 2104598 (2022).
- G. Chen, X. Liu, J. An, S. Wang, X. Zhao, Z. Gu, C. Yuan, X. Xu, J. Bao, H.-S. Hu, J. Li, X. Wang, Nucleation-mediated growth of chiral 3D organic-inorganic perovskite single crystals. Nat. Chem. 15, 1581–1590 (2023).

- Q. Guan, T. Zhu, Z.-K. Zhu, H. Ye, S. You, P. Xu, J. Wu, X. Niu, C. Zhang, X. Liu, J. Luo, Unprecedented chiral three-dimensional hybrid organic-inorganic perovskitoids. *Angew. Chem. Int. Ed.* 62, e202307034 (2023).
- M. Li, F. Fang, X. Huang, G. Liu, Z. Lai, Z. Chen, J. Hong, Y. Chen, R.-J. Wei, G.-H. Ning, K. Leng, Y. Shi, B. Tian, Chiral ligand-induced structural transformation of low-dimensional hybrid perovskite for circularly polarized photodetection. *Chem. Mater.* 34, 2955–2962 (2022)
- Y. Zhao, X. Li, J. Feng, J. Zhao, Y. Guo, M. Yuan, G. Chen, H. Gao, L. Jiang, Y. Wu, Chiral 1D perovskite microwire arrays for circularly polarized light detection. *Giant* 9, 100086 (2022).
- A. Maiti, A. J. Pal, Spin-selective charge transport in lead-free chiral perovskites: The key towards high-anisotropy in circularly-polarized light detection. *Angew. Chem. Int. Ed.* 61, e202214161 (2022).
- J. Hao, H. Lu, L. Mao, X. Chen, M. C. Beard, J. L. Blackburn, Direct detection of circularly polarized light using chiral copper chloride–carbon nanotube heterostructures. ACS Nano 15, 7608–7617 (2021).
- T. Liu, W. Shi, W. Tang, Z. Liu, B. C. Schroeder, O. Fenwick, M. J. Fuchter, High responsivity circular polarized light detectors based on quasi two-dimensional chiral perovskite films. ACS Nano 16, 2682–2689 (2022).
- X. Zhang, X. Liu, L. Li, C. Ji, Y. Yao, J. Luo, Great amplification of circular polarization sensitivity via heterostructure engineering of a chiral two-dimensional hybrid perovskite crystal with a three-dimensional MAPbl<sub>3</sub> Crystal. ACS Cent. Sci. 7, 1261–1268 (2021).
- W. Wu, X. Shang, Z. Xu, H. Ye, Y. Yao, X. Chen, M. Hong, J. Luo, L. Li, Toward efficient two-photon circularly polarized light detection through cooperative strategies in chiral quasi-2D perovskites. *Adv. Sci.* 10, 2206070 (2023).
- J. Wu, X. Zhang, S. You, Z.-K. Zhu, T. Zhu, Z. Wang, R. Li, Q. Guan, L. Liang, X. Niu, J. Luo, Low detection limit circularly polarized light detection realized by constructing chiral perovskite/Si heterostructures. Small 19, e2302443 (2023).
- X. Zhang, H. Ye, L. Liang, X. Niu, J. Wu, J. Luo, Direct detection of near-infrared circularly polarized light via precisely designed chiral perovskite heterostructures. ACS Appl. Mater. Interfaces 14, 36781–36788 (2022).
- C.-C. Fan, X.-B. Han, B.-D. Liang, C. Shi, L.-P. Miao, C.-Y. Chai, C.-D. Liu, Q. Ye, W. Zhang, Chiral rashba ferroelectrics for circularly polarized light detection. *Adv. Mater.* 34, e2204119 (2022).
- T. Zhu, H. Wu, C. Ji, X. Zhang, Y. Peng, Y. Yao, H. Ye, W. Weng, W. Lin, J. Luo, Polar photovoltaic effect in chiral alternating cations intercalation-type perovskites driving self-powered ultraviolet circularly polarized light detection. *Adv. Opt. Mater.* 10, 2200146 (2022).
- W. Wu, L. Li, D. Li, Y. Yao, Z. Xu, X. Liu, M. Hong, J. Luo, Tailoring the distinctive chiral-polar perovskites with alternating cations in the interlayer space for self-driven circularly polarized light detection. *Adv. Opt. Mater.* 10, 2102678 (2022).
- Y. Liu, Y. Jiang, Z. Xu, L. Li, D. Zhang, W. Zheng, D. Liang, B. Zheng, H. Liu, X. Sun, C. Zhu, L. Lin, X. Zhu, H. Duan, Q. Yuan, X. Wang, S. Wang, D. Li, A. Pan, Magnetic doping induced strong circularly polarized light emission and detection in 2D layered halide perovskite. Adv. Opt. Mater. 10, 2200183 (2022).
- Y. Zhao, M. Dong, J. Feng, J. Zhao, Y. Guo, Y. Fu, H. Gao, J. Yang, L. Jiang, Y. Wu, Lead-free chiral 2D double perovskite microwire arrays for circularly polarized light detection. *Adv. Opt. Mater.* 10, 2102227 (2022).
- J. Wang, H. Lu, X. Pan, J. Xu, H. Liu, X. Liu, D. R. Khanal, M. F. Toney, M. C. Beard, Z. V. Vardeny, Spin-dependent photovoltaic and photogalvanic responses of optoelectronic devices based on chiral two-dimensional hybrid organic-inorganic perovskites. ACS Nano 15, 588–595 (2021).
- Z. Liu, C. Zhang, X. Liu, A. Ren, Z. Zhou, C. Qiao, Y. Guan, Y. Fan, F. Hu, Y. S. Zhao, Chiral hybrid perovskite single-crystal nanowire arrays for high-performance circularly polarized light detection. *Adv. Sci.* 8, 2102065 (2021).
- J. Wang, C. Fang, J. Ma, S. Wang, L. Jin, W. Li, D. Li, Aqueous synthesis of low-dimensional lead halide perovskites for room-temperature circularly polarized light emission and detection. ACS Nano 13, 9473–9481 (2019).

#### Acknowledgments

Funding: This work was supported by the National Research Foundation of Korea (NRF) grant (RS-2024-00398065, 2023R1A2C3007715, and RS-2023-00257666) through the NRF by the Ministry of Science and ICT (MSIT), Korea. This work was also supported by Korea Toray Science Foundation. The Institute of Engineering Research at Seoul National University provided research facilities for this work. The computational resources were provided by the Korea Institute of Science and Technology Information (KISTI) (KSC-2023-CRE-0497) and UNIST-HPC. Author contributions: H.K. and W.C. designed and conducted the study under the supervision of J.H.O. H.K. and W.C. fabricated samples for chiroptical analyses, performed thin-film characterization, and conducted device analyses under the supervision of J.H.O. Y.J.K. conducted amilation studies under the supervision of S.K.K. Ji.K. conducted and interpreted TEM measurements under supervision of Ju.P., Jo.P., J.A., and I.S. helped with device measurements under the supervision of J.H.O., M.K. and J.O.K. helped with the synthesis of chiral molecules under the supervision of D.Y., H.K., W.C., Y.J.K., S.K.K., and J.H.O. wrote the

manuscript. All authors discussed the results and commented on the manuscript. **Competing interests:** The authors declare that they have no competing interests. **Data and materials availability:** All data needed to evaluate the conclusions in the paper are present in the paper and/or the Supplementary Materials.

Submitted 9 February 2024 Accepted 16 July 2024 Published 21 August 2024 10.1126/sciadv.ado5942